South African Journal of Geomatics, Vol. 11. No. 1, February 2022

Estimating the performance of multi-rotor unmanned aerial vehicle structure-from-motion (UAV_{sfm}) imagery in assessing homogeneous and heterogeneous forest structures: a comparison to airborne and terrestrial laser scanning

Kenechukwu C. Onwudinjo[1], Julian Smit[2]

Geomatics Division, Department of Architecture, Planning and Geomatics, Faculty of Engineering & the Built Environment, University of Cape Town, Cape Town, South Africa, [1]kconwudinjo@outlook.com, [2]Julian.Smit@uct.ac.za

DOI: http://dx.doi.org/10.4314/sajg.v11i1.6

Abstract

The implementation of Unmanned Aerial Vehicles (UAVs) and Structure-from-Motion (SfM) photogrammetry in assessing forest structures for forest inventory and biomass estimations has shown great promise in reducing costs and labour intensity while providing relative accuracy. Tree Height (TH) and Diameter at Breast Height (DBH) are two major variables in biomass assessment. UAV-based TH estimations depend on reliable Digital Terrain Models (DTMs), while UAV-based DBH estimations depend on reliable dense photogrammetric point cloud. The main aim of this study was to evaluate the performance of multi-rotor UAV photogrammetric point cloud in estimating homogeneous and heterogeneous forest structures, and their comparison to more accurate LiDAR data obtained from Aerial Laser Scanners (ALS), Terrestrial Laser Scanners (TLS), and more conventional means like manual field measurements. TH was assessed using UAV_{SfM} and LiDAR point cloud derived DTMs, while DBH was assessed by comparing UAV_{SfM} photogrammetric point cloud to LiDAR point cloud, as well as to manual measurements. The results obtained in the study indicated that there was a high correlation between UAV_{SfM} TH and ALS_{LiDAR} TH (R^2 = 0.9258) for homogeneous forest structures, while a lower correlation between UAV_{SfM} TH and TLS_{LiDAR} TH (R^2 = 0.8614) and UAV_{SfM} TH and ALS_{LiDAR} TH (R^2 = 0.8850) was achieved for heterogeneous forest structures. A moderate correlation was obtained between UAV_{SfM} DBH and field measurements (R^2 = 0.5955) for homogenous forest structures, as well as between UAV_{SfM} DBH and TLS_{LiDAR} DBH (R^2 = 0.5237), but a low correlation between UAV_{SfM} DBH and UAV_{LiDAR} DBH (R^2 = 0.1114). The study demonstrated that UAV acquired imagery can be used to accurately estimate TH in both forest types, but has challenges estimating DBH. The research does not suggest that UAV_{SfM} serves as a replacement for more high-cost and accurate LiDAR data, but rather as a cheaper adequate alternative in forestry management depending on accuracy requirements.

Keywords: *Unmanned Aerial Vehicles, Structure-from-Motion, Aerial Laser Scanning, Terrestrial Laser Scanning, Tree Height, Diameter at Breast Height, Biomass*

1. Introduction

Many developing countries rely on National Forest Inventories (NFIs) for their biomass and carbon stock estimates (Kachamba *et al*., 2016). An effort to be part of The Reducing Emissions from Deforestation and forest Degradation plus forest conservation, sustainable management of forest and enhancement of forest carbon stocks (REDD+) mechanism, as it provides developing countries the financial incentive for reducing forest degradation and deforestation. One of the requirements to benefit from the REDD+ mechanism is that participating countries of the United Nations Framework Convention on Climate Change (UNFCCC) report their verified national biomass and carbon estimates. It is therefore expected of these countries to have capable systems for carbon monitoring and technologies or methodologies with which to obtain this data. Unfortunately, many of these countries do not have comprehensive NFIs, which are run at high operational cost and are highly labour intensive. Due to these limitations in the conventional acquisition of the necessary measurements and subsequent estimation of biomass, Remote Sensing has played a vital role in the last few decades with estimating above ground biomass more efficiently and cost effectively (Günlü *et al*., 2014).

Remote Sensing has been used extensively in forest management and monitoring as it provides observations over a large area, can be repeated with ease after the initial application, and thereby offering a time saving alternative. Techniques such as the use of satellite imagery are a popular, inexpensive, and a valuable alternative to conventional field measurement methods (Maina *et al.*, 2017). However, satellite imagery is usually flawed with relatively poor spatial resolution, and is periodically captured with extensive cloud cover, making processing challenging. Radio Detection and Ranging (RADAR), Aerial Laser Scanning (ALS), Terrestrial Laser Scanning (TLS), and optical images such as satellite imagery or large scale photography have proven to be a useful as a substitute to conventional methods, but are expensive, labour intensive, and time-consuming (Brede *et al*., 2017). These systems have been widely used in forest management with varying success due to differences in vegetation types, environmental conditions, forest canopy cover, and differences in the methods used (Kachamba *et al*., 2016).

For instance, RADAR systems such as Space-borne Synthetic Aperture RADAR (SAR) have the advantage of being able to operate regardless of weather and daylight and are able to penetrate forest canopies. However, challenges exist with polarization, land cover, terrain properties, and the incidence angle of the sensor (Maina *et al*., 2017), as well as poor spatial resolution. Distinguishing vegetation types is also a challenge for RADAR as it is also hampered by poor spectral resolution. ALS and TLS are also weather and daylight independent, and have shown great potential for forest inventory acquisition and biomass estimation in varying forest structures (Iizuka *et al*., 2018; Kachamba *et al*., 2016). ALS, however, often has difficulty with adequately capturing below-canopy forest structures such as complete tree trunks in very dense forests, depending on the sensor used, while TLS boasts of the ability to capture below-canopy forest structures but falls short at capturing the top of the forest canopy (Wilkes *et al*., 2017). Both can be labour intensive, costly, and time consuming (Brede *et al*., 2017).

Unmanned Aerial Vehicles (UAVs) have been utilised over the last few decades in numerous surveying and monitoring applications. They have garnered subsequent use in forestry management in recent years, especially with the use of Structure-from-Motion (SfM) photogrammetry and readily available stereo-matching software in estimating forest variables in *Pinus* forests with relative success (Guerra-Hernández et al., 2016; Galidaki et al., 2017; Mlambo et al., 2017). Low altitude UAV imagery was used to assess forest canopy height (Lisein *et al*., 2013), used to generate regression models to calculate individual tree biomass (Jones *et al*., 2007), and used to produce digital surface models using photogrammetric methods (St-Onge *et al*., 2008). UAV imagery was also used to estimate biomass in dry woodlands of Malawi (Kachamba *et al*., 2016), to estimate Japanese Cypress (*Chamaecyparis obtusa*) TH and DBH from digital surface models and orthophotos using UAV_{SfM} imagery (Iizuka *et al*., 2018), and to compare UAV_{SfM} derived point cloud data of tree variables to LiDAR data (Puliti *et al*., 2015).

Although UAVs and SfM have been used successfully in these studies, they are not without flaws in their results, although marginal. Puliti *et al*., (2015) recorded correlations of $R^2 = 0.710$, $R^2 = 0.970$, $R^2 = 0.600$, $R^2 = 0.600$, and $R^2 = 0.850$ for the variables Lorey's Mean Height (hL), Dominant Height (hdom), Stem Number (N), Basal Area (G), and Stem Volume (V) respectively, but only after combining SfM and ALS data due to a deficiency in ground imagery data resulting from UAV_{SfM} only achieving limited penetration of top-canopy forests. This is a known limitation with SfM. Iizuka *et al*., 2018 obtained $R^2 = 0.2076$ when estimating the relationship between SfM estimated TH and observed field measured TH of a dense and mature (planted in 1959) Japanese Cypress forest, $R^2 = 0.7786$ between canopy width and DBH, and $R^2 = 0.7923$ between canopy area and DBH. Guerra-Hernández *et al*., (2016) achieved a correlation of $R^2 = 0.810$ when comparing low-cost UAV_{SfM} derived TH to field measured TH in their 2016 study of a 23-year-old *Pinus pinea* forest plantation.

From the studies mentioned above, it is evident that the accuracy of forest variables, such as TH, is dependent on the ability of the sensor to acquire not only above canopy forest structures, but below canopy forest structures as well, such as the ground. As such, the accuracy of TH estimations, for example, is a function of an accurate Digital Terrain Model (DTM). ALS sensors are able to acquire this with ease, as they are airborne sensors and the narrow laser beams are able to penetrate the small gaps between the vegetation, and while TLS can also achieve this it requires more manoeuvring around obstacles and a number of setups. A photogrammetric point cloud can be obtained of dense forests; however, this is often limited to the top canopy as no narrow laser beams are used here to penetrate the small gaps in the vegetation. Photographically derived terrain model data requires stereo image coverage, which is unlikely in areas with dense tree canopy structures. Oblique imagery can be incorporated to acquire additional below-canopy structures. In addition to nadir and oblique imagery, tessellated façade aerial imagery was incorporated, as was done by Carnevali *et al*., (2018) when using UAVs and photogrammetry for modelling historical buildings for architectural purposes. The tessellated façade imagery served as an alternative to terrestrial photography using DSLR cameras to acquire sufficient below-canopy forest structure data, thereby creating a completely UAV-reliant approach in acquiring forestry data.

When estimating TH and DBH using photogrammetric point cloud data, several phases are involved. For TH, the point cloud needs to be classified into ground and non-ground (vegetation etc.) points. After which, the ground points can be used to create a continuous ground surface (DTM), the ground and non-ground points can be used to create a Digital Surface Model (DSM) which shows the elevation of all present structures. After which, a Canopy Height Model (CHM) can be created which shows the absolute height of any present structures thereby resulting in the TH (Brede *et al*., 2017). As for DBH, the measurements can be extracted from the photogrammetric point cloud 1.37m above the ground level (Malone *et al*., 2009), or the trunks modelled into cylinders and their diameters extracted (Olofsson and Holmgren, 2017).

ALS and TLS LiDAR data are generally considered to be the best for creating DTMs and extracting forest variables (Brede *et al*., 2017; Colomina and Molina, 2014) as they are more reliable and technologically better suited to data capture in dense forest structure environments. However, these technologies can incur high costs. UAV_{SfM} may offer a cheaper alternative to this, within limits.

2. Materials and Methods

2.1. The Study Area

The three study areas, $H_{omo}FS$, $H_{etero}FS_1$, and $H_{etero}FS_2$, located at Rondebosch Common, the University of Cape Town, and Steenbras Dam Nature Reserve respectively, chosen for this research project are located in Cape Town (Figure 1), which lies along the western coastline of the Western Cape province of South Africa at latitude 33°55'33.0" S, longitude 18°25'23.6" E, approximately 30m above mean sea level. Cape Town was chosen because of its unique climate in comparison to the rest of the country. It has a winter rainfall Mediterranean climate compared to the subtropical summer rainfall climate experienced by the rest of the country (Tuswa *et al*., 2019). This makes Cape Town, and the Western Cape as a whole, a unique location for the growth of several vegetation types, including woody homogeneous and heterogeneous *Pinus* forest structures, that are unique to this region of South Africa, and the world. $H_{omo}FS$, $H_{etero}FS_1$, and $H_{etero}FS_2$ were planned at each of the respective study areas as Regions of Interest (ROIs).

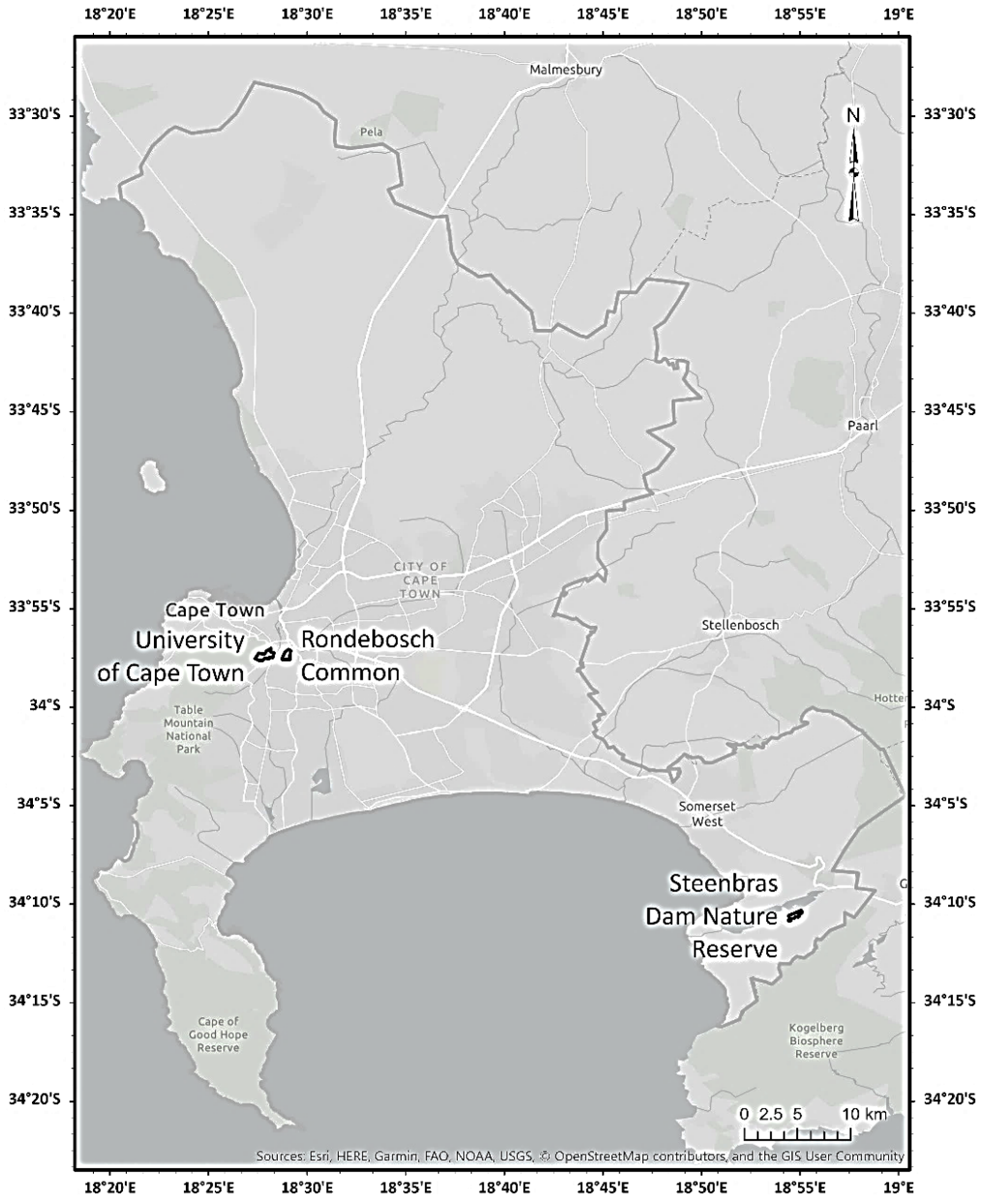

Figure 1. The location of the study areas and their relative location to each other.

2.2. Equipment

The data used in this research endeavour include 20MP 5472 x 3648 pixel nadir and oblique RGB UAV aerial imagery acquired using a DJI Phantom 4 Pro (Figure 2c), LiDAR data acquired with a Riegl miniVUX®-1UAV LiDAR sensor attached to a DJI Matrice 600, LiDAR data acquired with a Z+F Imager® 5010X laser scanner (Figure 2b), coordinates acquired with a Trimble R4 dGNSS (Figure 2a), and high-altitude low-resolution LiDAR data acquired from the City of Cape Town Municipality through the University of Cape Town. Conventional field measured DBH data was also collected at $H_{omo}FS$ for comparison to UAV_{SfM}.

Figure 2. (a) Trimble R4 dGNSS, (b) Z+F Imager® 5010X laser scanner, (c) DJI Phantom 4 Pro Quadcopter

2.3. Data Collection

2.3.1. Design, Field Measurement and Ground Control Collection

Field measurements were applied when measuring the DBH for trees at $H_{omo}FS$ (Rondebosch Common), while at the other two sites, $H_{etero}FS_1$ (University of Cape Town) and $H_{etero}FS_2$ (Steenbras Dam), DBH was collected using TLS (TLS_{LiDAR}), ALS (ALS_{LiDAR}) and a UAV with ALS (UAV_{LiDAR}). The circumference of 30 trees with DBH ≥ 5cm at $H_{omo}FS$ were collected on 20 June 2018, using a measuring tape wrapped around each tree trunk 1.37m above ground level (Malone *et al.*, 2009). The DBH was calculated using an allometric equation, Equation 1, suggested by González-Jaramillo *et al*, (2019), where d is the tree diameter c is the tree circumference, and π is equal to 3.14:

$$d = \frac{c}{\pi} \quad [1]$$

Ground Control Points (GCPs) were included for each UAV_{SfM} survey of each site to aid in correcting shifts and distortions due to possible loss of, or poor, Inertial Measurement Unit (IMU) and Global Navigation Satellite System (GNSS) measurements recorded by the UAV during flight (Puliti, 2017), and possibly improve overall image registration (Dandois *et al*., 2015). Easily identifiable features such as road markings or curb corners were identified as possible GCP markers where possible. Where no easily identifiable features existed, GCPs in the form of 1m by 1m black and white checkered mats were used as easily identifiable features to be captured in the UAV imagery. To achieve this, 30cm long 10mm round iron pegs were hammered into desired positions and the mat centres aligned with the pegs. The centres of the mats were surveyed for their precise vertical and horizontal positions. In this study, all GCPs were surveyed using a Trimble R4 differential Global Navigation Satellite System (dGNSS) unit. The dGNSS unit comprised of two Trimble R4 receivers, a base receiver, and a rover receiver. Both receivers were set to observe pseudo-range and carrier phase signals of Global Positioning System (GPS) and Global Navigation Satellite System (GLONASS) to provide the precise positions of the GCPs. Three different GNSS survey styles were used in this study. At $H_{omo}FS$, a base was established, and the rover was used to navigate to and

survey in the positions of three Town Survey Marks (TSMs) around the area, as well as the GCPs in Real-time Kinematic (RTK) mode on 20 June 2018. At $H_{etero}FS_1$, a Virtual Reference Station (VRS) was used to reference the surveyed GCPs to a network of Trigonometrical Beacons (Trigs) on the Continuous Operating Reference Stations (CORS) also in RTK mode on 12 February 2019. Finally, at $H_{etero}FS_2$, a static survey was done as VRS was not available, nor were there any physical reference stations nearby to reference the survey to. This survey was done on 19 July 2018. The average baseline distances were 40km to any Trigs. GCPs were surveyed in Fast-Static and processed along with the base station later using Trimble Business Center (Trimble Geospatial, 2021). All GCPs were surveyed within deviations of 0.03m on the horizontal and vertical positions. Independent Check Points (CPs) were also surveyed to within 0.03m at $H_{omo}FS$ and $H_{etero}FS_1$ as there were either TSMs or local control available in the area. This was however not possible at $H_{etero}FS_2$ as there were no CPs available in the area.

2.3.2. Collection of UAV Imagery

Nadir and Oblique UAV imagery at $H_{omo}FS$ was acquired on three different days: 20 June 2018, 22 June 2018, and 18 July 2018. Nadir and Oblique UAV imagery was also captured over two days for $H_{etero}FS_1$, with the tessellated façade imagery being captured on a third day: 12 February 2019, 23 February 2019, and 10 May 2019; while for $H_{etero}FS_2$, nadir and oblique imagery were captured over five days: 19 June 2018, 31 August 2018, 4 October 2018, 10 December 2018, and the 7 February 2019. Due to logistical challenges, image acquisition for the $H_{etero}FS_2$ site was not always possible, hence the big gaps between the acquisition dates. This is a potential operational challenge, and as such lighting and shadow effects can be expected. During the study, measures were taken to fly under identical weather conditions and around noon to keep lighting effects on the image quality marginal and limit the presence of shadows. All UAV_{SfM} imagery were acquired using a DJI Phantom 4 Pro (DJI, 2017) (Figure 2c), equipped with a 5472 x 3648 pixel RGB sensor that captures 20 megapixel images in the red, green and blue spectral bands. The camera shutter speed was set to 1/2000s. The Phantom 4 Pro weighs approximately 1388g as a unit, and is equipped with an IMU, and an on-board GNSS to assist with flight and autonomous positioning (DJI, 2017).

Before every take-off for each survey, the mats were laid out over the peg positions and the corners fastened to the ground, and the take-off and landing zones were cleared of obstructions, e.g., by positioning the take-off and landing zone away from the tree edge. Since the GCPs were surveyed in the initial ground control survey, there was no need to survey them again. All the nadir and oblique flights were planned, and executed, on a Samsung Galaxy Note 5 smartphone with Pix4D Capture (Pix4Dcapture, 2019) (Figure 3). In all UAV_{SfM} flights, forward lap and side lap were set to 80% to ensure adequate overlap of subsequent imagery, and due to South African Civil Aviation Authority (SACAA) regulations on safe and acceptable operations of a Remotely Piloted Aircraft System (RPAS), no flight was planned for, or flown, above 120m (400ft) above ground level (AGL) (SACAA, 2021). Table 1 below summarises the nadir flight parameters for each study area, while Table 2 shows that of the oblique flight parameters. Images flown at higher AGL provided a wider

scene for more features to be used in the image matching phase, while the images acquired at lower AGL provided higher resolution imagery for finer detail.

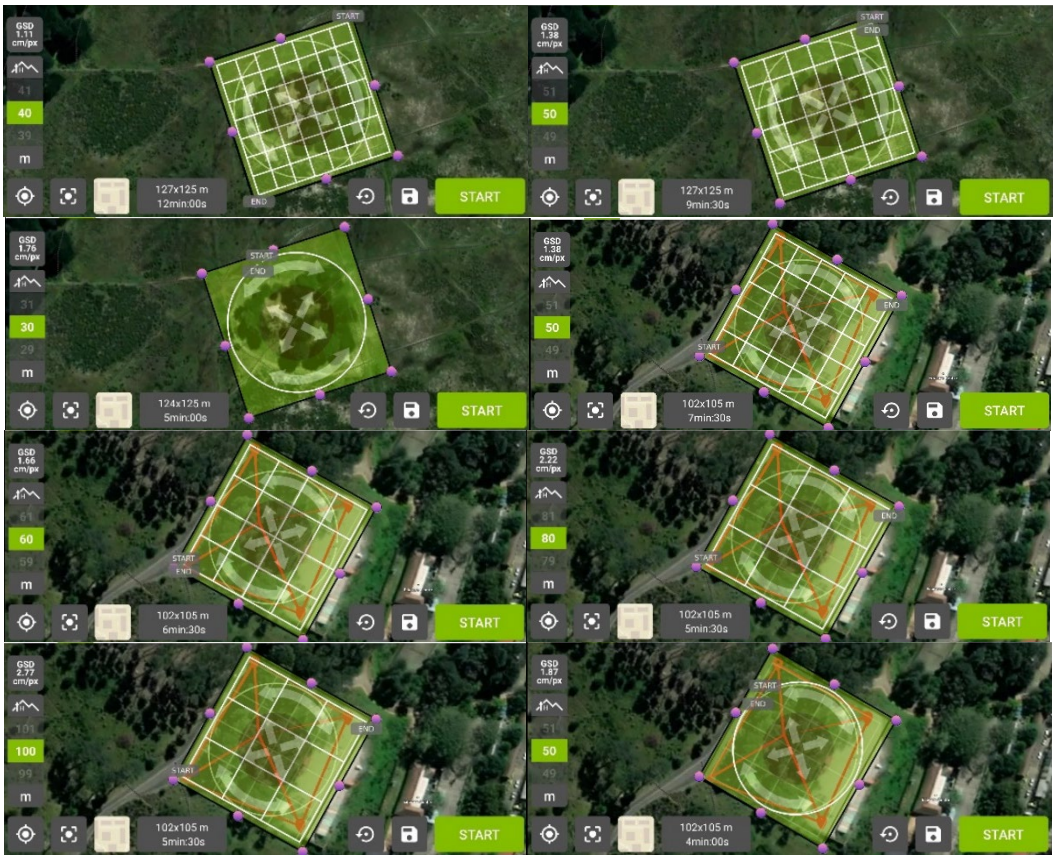

Figure 3. Pix4Dcapture flight plans. (a) – (b) Double Grid Nadir flight for $H_{omo}FS$, (c) Circular Oblique flight for $H_{omo}FS$, (d) – (g) Double Grid Nadir flight for $H_{etero}FS_1$, and (h) Circular Oblique flight for $H_{etero}FS_1$

Table 1. Flight plan specifications for nadir double grid flights of the study areas

Parameters	**Values**		
	HomoFS	***HeteroFS1***	***HeteroFS2***
Flight Altitude (AGL)	40m and 50m	50m, 60m, 80m and 100m	35m, 50m and 100m
Total Approx. Flight Time	17 min	19 min	42 min
Size/Area	125m by 125m	102m by 105m	115m by 160m
GSD	1.10-1.37cm/pix	1.37-2.74cm/pix	0.96-2.74cm/pix
Front and Side Overlap	80%	80%	80%
Flight Speed	5m/s	5m/s	5m/s
Camera Angle	90°	90°	90°
Approx. Number of Images	402	361	826

Table 2. Flight plan specifications for oblique flights of the study areas

Parameters	Values		
	$H_{omo}FS$	***$H_{etero}FS_1$***	***$H_{etero}FS_2$***
Flight Altitude (AGL)	20m and 30m	50m	30m, 50m and 60m
Total Approx. Flight Time	8 min	4 min	26 min
Size/Area	125m by 125m	102m by 105m	115m by 160m
GSD	1.66-1.77cm/pix	1.86cm/pix	1.87-2.35cm/pix
Capture Angle	10°	10°	10°
Flight Speed	3m/s	3m/s	3m/s
Camera Angle	35° and 45°	90°	90°
Approx. Number of Images	247	88	360

The tessellated façade flight was flown manually as there exists no automated flight plan on either Pix4D Capture or DJI Go 4 app (DJI, 2021), the native DJI flight app, for a tessellated façade flight pattern. Each flight line was planned and flown 2m apart, with an image captured every second. These parameters were implemented to ensure as much image overlap to acquire as much below-canopy detail as possible. Carnevali et al., (2018) used a similar flight pattern in surveying building façades for architectural purposes (p. 220). A summary of the flight specifications for the tessellated façade flight plan for $H_{etero}FS_1$ is shown in Table 3.

Table 3. Flight plan specifications for tessellated flight

Parameters	Values
	$H_{etero}FS_1$
Flight Altitude (AGL)	2m - 15m
Total Approx. Flight Time	1 hour 5 min
Total Horizontal Baseline	85m
Vertical Baselines (each)	15m
GSD	0.41cm/pix
Flight Speed	3m/s
Camera Angle	0° - 30°
Approx. Number of Images	1255

2.3.3. Terrestrial Laser Scanning Data Collection

TLS LiDAR data was acquired for both $H_{etero}FS_2$ and $H_{etero}FS_1$ on 26 April 2019 and 10 May 2019 respectively. However, the survey of $H_{etero}FS_2$ was discarded for various reasons – some targets placed on the tree trunks fell off the trunks during the survey, making referencing between stations challenging; rampant subspecies below-canopy growth obstructed line-of-sight between some targets and the scan positions; the absence of distinct features in a monotonous environment also proved to be a challenge for referencing scans; and the thick forest top-canopy was a challenge for the in-built GPS to receive satellite signals to assist with instrument orientation and referencing. These challenges meant that the scans could not be registered with high enough accuracy and low enough residuals to constitute an accurate and successful survey; a return to site to repeat the survey was also not possible within a reasonable timeframe. The scans were acquired using Z+F Imager® 5010X Terrestrial Laser Scanner (Zoller + Fröhlich, 2020). The scanner, which weighed a total of 11kg with the battery included, was equipped with an IMU and a GNSS.

Several A4 sheets with opposing black triangles were taped onto as many tree trunks as possible to maximise the chances of clear line of sight between scan positions, while some A4 sheets were placed on easily identifiable positions on the parking bays. Some of these markers were used as CPs to validate the accuracy of the generated point cloud and models. The mats used in the UAV_{SfM} surveys were also placed on their respective positions to be surveyed during the LiDAR survey to assist with registration of the scans. A total of 44 targets were initially placed throughout $H_{etero}FS_1$ to assist with referencing the images on both the horizontal and vertical plane, however (González-Jaramillo *et al*., 2019) argues that no more than 6 targets are necessary. Scan registration was done in Z+F LaserControl® v9.0.2.24038 (Zoller + Fröhlich, 2020), and cleaning in Autodesk Recap v6.0.0 (Autodesk, 2021). Table 4 shows the TLS registration statistics.

Table 4. Statistics on the TLS registration of $H_{etero}FS_1$

Total number of targets (A4 sheets and supplementary features)	148
Number of disabled targets	5
Average Deviation	15.1mm
Standard Deviation	8.5mm
Maximum Deviation	48.5mm

2.4. Image Processing

Agisoft Metashape v1.5.1 (Agisoft, 2017) was used to generate the photogrammetric point cloud for all the UAV_{SfM} acquired imagery, as the software utilises both SfM and stereo-matching algorithms for multi-view stereo reconstruction and image alignment. Several phases were involved in obtaining the photogrammetric point cloud: (1) built-in SfM algorithms aligned the imagery; (2) a sparse cloud of the scene was created; (3) markers were placed over the GCPs and their precise GPS positions were imported to improve orientation and positioning; (4) the camera alignment was optimised (Figure 5.); (5) a colourised dense point cloud of the scene was created; (6) and an RGB orthophoto of the scene was finally created. The processes followed were similar to those followed by (Puliti *et al*., 2015; Kachamba *et al*., 2016). Automated batch files in the software were created for each of the nadir, oblique and the tessellated façade imagery datasets to speed up processing. These individual point clouds were later combined into one dense point cloud (Figure 4). Processing was done on a Lenovo Y70 (Lenovo, 2020) Intel® Core™ i7 processor, NVIDIA® GTX-860M with 4G VRAM graphics card, and 16GB DDR3L RAM high performance gaming laptop.

Figure 4. Dense point cloud of $H_{etero}FS_1$ showing coherent measurable tree structures

Figure 5. Image positions of the captured nadir and oblique images over the dense cloud of $H_{omo}FS$

Due to extensive invasion of below canopy subspecies which caused numerous challenges including shadows and obstruction of tree trunks, the photogrammetric point cloud for $H_{etero}FS_2$ was discarded after several attempts failed to reprocess the dataset for more favourable results.

2.5. Generation of DTMs

Digital Terrain Models were created for $H_{omo}FS$ and $H_{etero}FS_1$ each using the UAV_{SfM} photogrammetric point cloud; as well as Digital Terrain Models using the ALS_{LiDAR} data: a 10cm Digital Surface Model (DSM), a 10cm Digital Elevation Model (DEM), and a 10cm Canopy Height Model (CHM) for each cloud dataset (Iizuka et al., 2018; Kachamba et al., 2016; Guerra-Hernández et al., 2016). Creating higher resolution terrain models, such as <10cm, would increase processing time. Various attempts using a grid spacing of lower than 10cm led to longer processing times and software crash. Both the LiDAR data and UAV_{SfM} photogrammetric

point cloud were classified into appropriate ground and non-ground (vegetation) point classes. The DEMs were modelled using both classified ground and non-ground point classes, while DSMs were modelled using only the classified ground point class (Figure 6). The CHM, which represents the absolute tree height, was the difference between the two (Lim et al., 2003; González-Jaramillo et al., 2019):

$$CHM = DEM - DSM \quad [2]$$

All the terrain models were created using the Triangulated Irregular Network (TIN) method to create a surface.

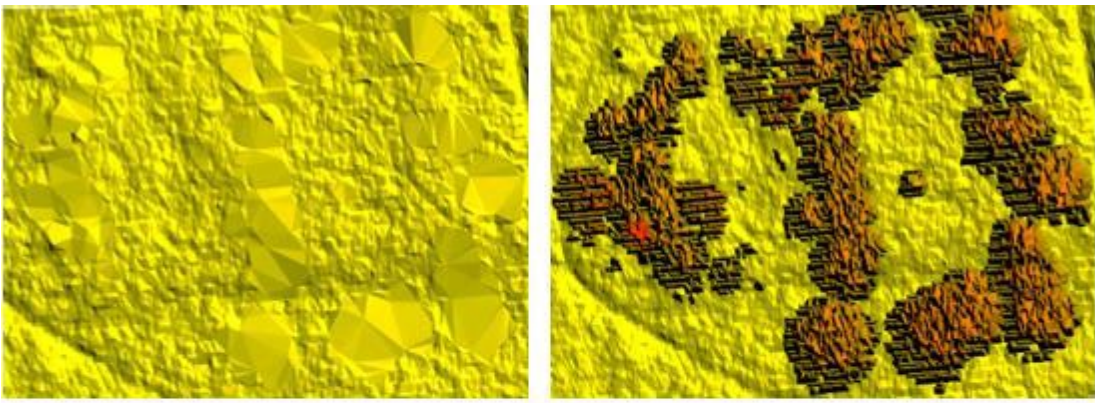

Figure 6. A 10cm DSM and a 10cm DEM of some of the trees in the H_{omo}FS area

2.6. Variable Extraction

2.6.1. DBH

All non-ground (vegetation) points above 1.37m (DBH) (Malone *et al*., 2009) and below 1.00m from the average ground level were temporarily reclassified into a random class, producing several vertical 0.37m long stem cylinders of vegetation points in the vegetation class that formed the trunks as was done by (Olofsson and Holmgren, 2017). These cylinders were used to measure the diameters of the tree trunks by extracting the best-fit circular or ellipsoidal vectors (Figure 7) around the vegetation points, and extracting the perpendicular measurements across the circles to obtain the average DBH (Brede *et al*., 2017). The cylinders were also used to mark the individual tree positions so their respective TH measurements could be extracted. Point features were created at the centre of each cylinder to mark its position. This procedure was repeated on all UAV_{SfM} photogrammetric point cloud data for H_{omo}FS and $H_{etero}FS_1$, as well as the TLS_{LiDAR} and UAV_{LiDAR} data acquired for $H_{etero}FS_1$. A total of 32 trees were assessed in the H_{omo}FS study area, while a total of 20 trees were assessed in the $H_{etero}FS_1$ study area.

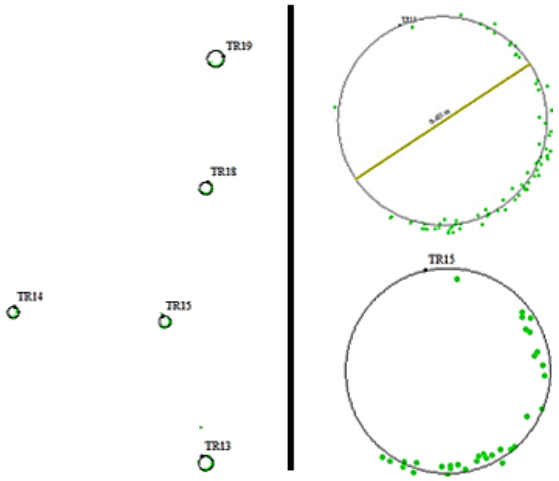

Figure 7. Best-fit vector data and DBH extracted from the tree vegetation point cloud of $H_{etero}FS_1$

2.6.2. TH Extraction

For each area, the TH was extracted from the modelled CHMs. When assessing TH in $H_{omo}FS$, both a 10cm resolution UAV_{SfM} point cloud derived CHM and a ALS_{LiDAR} data CHM were used. When assessing TH in $H_{etero}FS_1$, three 10cm derived CHMs were used: a UAV_{SfM} point cloud derived CHM, a TLS_{LiDAR} data derived CHM, and a ALS_{LiDAR} data derived CHM. A total of 30 trees were assessed in the $H_{omo}FS$ dataset, while 20 trees were assessed in the $H_{etero}FS_1$ dataset. The average individual TH was extracted by measuring perpendicular distances across each relative tree position on each CHM.

2.7. Evaluating the performance of UAV_{SfM} derived tree variables

Various statistical tools were applied to evaluate the utility of UAV_{SfM}-derived point cloud against LiDAR data in assessing DBH and TH. Pearson's correlation (Pearson's *r*) outlined in Equation 3, (Maina *et al*., 2017; Jayathunga *et al*., 2018; Kachamba *et al*., 2016) was used extensively on the results to measure how well the various UAV_{SfM} datasets relate to their LiDAR dataset counterparts – the strength of the relationship between both variables:

$$\boldsymbol{r} = \frac{\boldsymbol{n}(\boldsymbol{\Sigma xy}) - (\boldsymbol{\Sigma x})(\boldsymbol{\Sigma y})}{\sqrt{[\boldsymbol{n}\boldsymbol{\Sigma x^2} - (\boldsymbol{\Sigma x})^2][\boldsymbol{n}\boldsymbol{\Sigma y^2} - (\boldsymbol{\Sigma y})^2]}} \quad [3]$$

where n is the total population number; x represents UAV_{SfM} DBH or TH values; and y represents the various LiDAR dataset DBH or TH values. The correlation coefficient formula shows a linear relationship between two sets of data being compared. The accuracy of Pearson's *r* obtained for the DBH and TH data was validated using the leave-one-out cross validation (CV) technique as suggested by (Jayathunga *et al*., 2018). The root mean square error (RMSE) of the data was also determined using Equation 4.:

$$RMSE = \sqrt{\frac{\Sigma_{i=1}^{n}(y_i - \hat{y}_i)^2}{n}} \quad [4]$$

where n is the number of samples, y_i; is the observed LiDAR DBH or TH value; and $\hat{y}_i$ is the UAV_{SfM} DBH or TH value. This was done to evaluate the average separation from the best-fit line of each sample measurement.

3. Results and discussion

3.1. UAV_{SfM} against TLS_{LiDAR}, UAV_{LiDAR} and Field Measured DBH

UAV_{SfM} DBH measurements were compared to field measured DBH values at $H_{omo}FS$ using a total of 32 sample trees in the area, while at $H_{etero}FS_1$ the same comparison was done but with TLS_{LiDAR} and UAV_{LiDAR} DBH data using 20 sample trees in both instances.

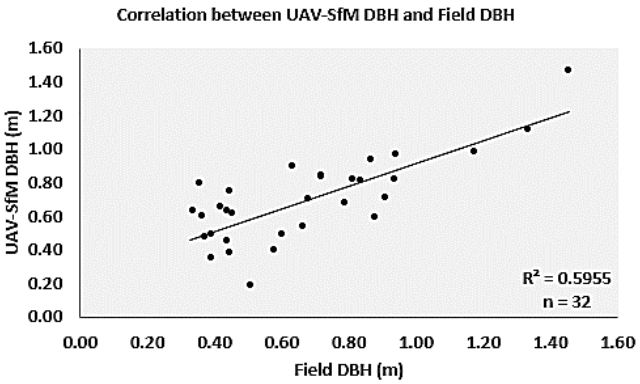

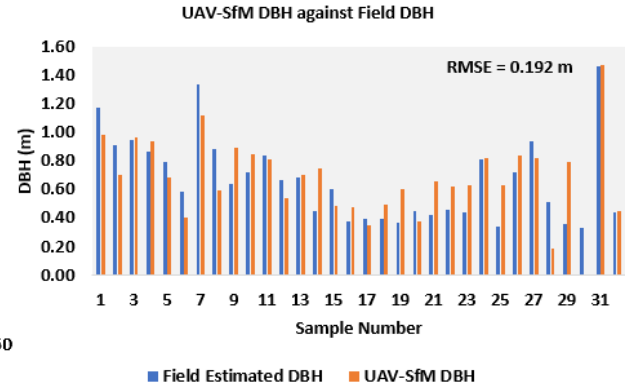

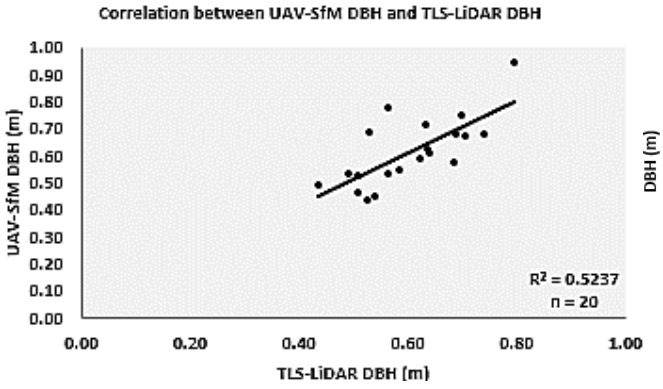

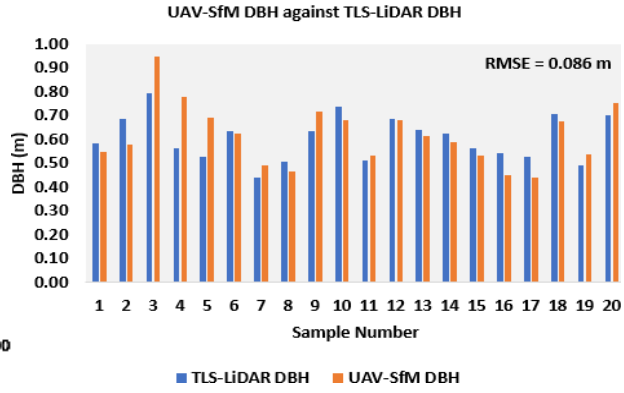

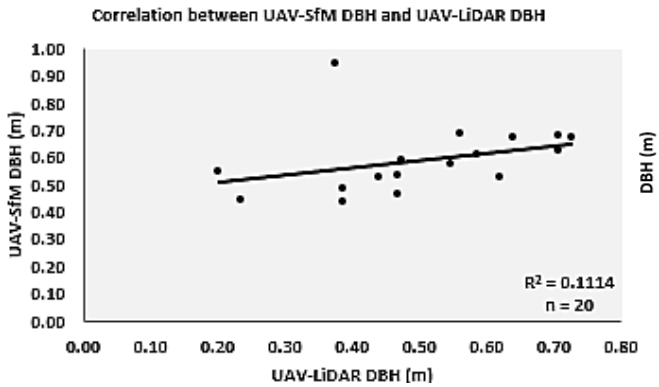

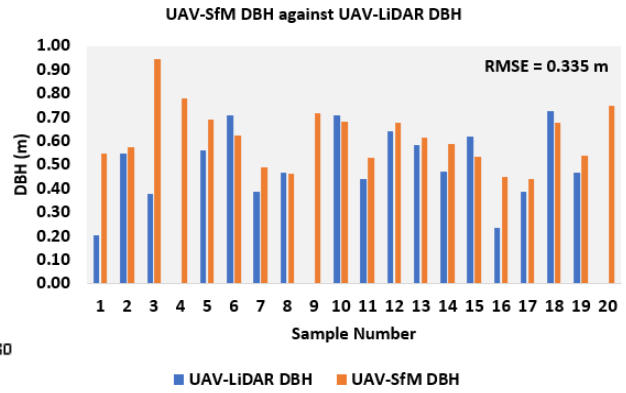

3.2. UAV_{SfM} against TLS_{LiDAR} and ALS_{LiDAR} TH

UAV_{SfM} TH measurements were compared to both TLS_{LiDAR} and ALS_{LiDAR} TH measurements. When assessing $H_{omo}FS$, 30 sample trees were used to evaluate the coefficient of determination between UAV_{SfM} and ALS_{LiDAR} data, while 20 sample trees were used in assessing the utility of UAV_{SfM} in estimating TH against TLS_{LiDAR} and ALS_{LiDAR} in $H_{etero}FS_1$.

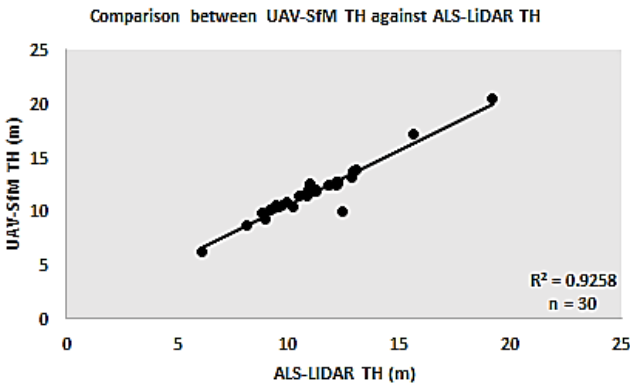

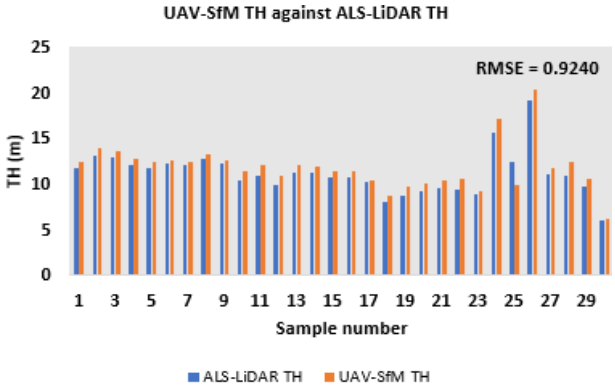

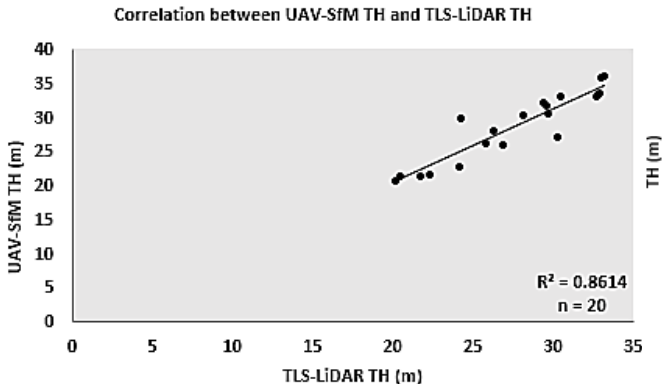

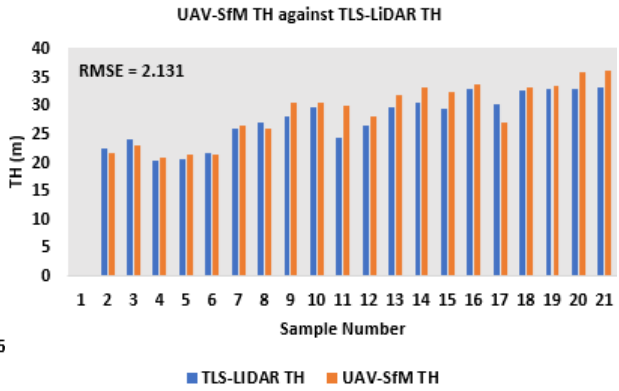

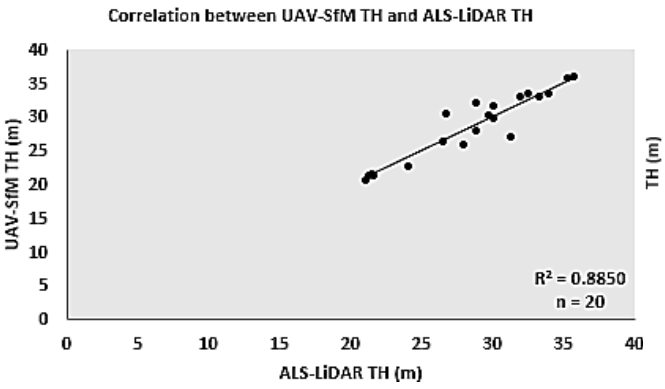

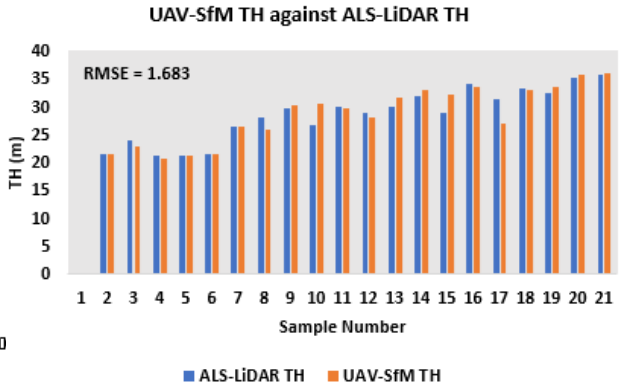

3.3. Discussion

For the DBH comparison, a moderate coefficient of determination of R^2 = 0.5955 (59.55%) was obtained, signifying UAV_{SfM} performs averagely well at estimating field DBH. A stark difference between the variables in the UAV_{SfM} and field measurements, minimum difference of 0.008m and

maximum difference of 0.438m, is suggestive of challenges in reconstructing full and accurate tree trunks in various instances using photogrammetry – a function of inadequate scene coverage caused by insufficient image cover from multiple perspectives. For the $H_{etero}FS_1$ comparison, a moderate agreement of R^2 = 0.5237 (52.37%) was also obtained when comparing UAV_{SfM} DBH to TLS_{LiDAR} DBH, while a poor agreement of R^2 = 0.1114 (11.14%) was obtained when comparing UAV_{SfM} DBH to UAV_{LiDAR} DBH (Figure 8). This was because the UAV_{LiDAR} data obtained failed to properly represent the full extent of some tree trunks making extraction of the actual diameter challenging, while LiDAR data for some trees were unavailable altogether. The poor relationship between the DBH values of the UAV_{SfM} and UAV_{LiDAR} comparison is made further apparent with the Pearson's r evaluation where the relationship had a value of r = 0.3337 (33.37%) signifying a large disparity between the measurements in the two datasets, compared to r = 0.7237 (72.37%) for UAV_{SfM} against TLS_{LiDAR}, and r = 0.7717 (77.17%) for UAV_{SfM} against field measurements. The RMSE for each data pair also highlighted the same indication with RMSE = 0.335m; RMSE = 0.086m; and RMSE = 0.192m for UAV_{SfM} against UAV_{LiDAR}, UAV_{SfM} against TLS_{LiDAR}, and UAV_{SfM} against field measurements, respectively.

An excellent correlation of R^2 = 0.9258 (92.58%) between UAV_{SfM} and ALS_{LiDAR} TH was obtained signifying that UAV_{SfM} performed well at estimating ALS_{LiDAR} TH. For UAV_{SfM} against TLS_{LiDAR}, a coefficient of determination of R^2 = 0.8614 (86.14%) was achieved, signifying a strong correlation between the two sets of data. A Pearson's r value of r = 0.9280 (92.80%) was also achieved, indicating a strong association between the two (Figure 9). However, a RMSE = 2.131m value was achieved for this comparison which shows the average separation from the line of best fit between these two variables, caused by the inability of TLS_{LiDAR} to properly acquire the top-canopy of the forest. On average, the UAV_{SfM} TH values were higher than the TLS_{LiDAR} values. When UAV_{SfM} was compared to ALS_{LiDAR}, a coefficient of determination of R^2 = 0.8850 (88.50%) was achieved, with a Pearson r value of r = 0.9407 (94.07%) and a RMSE = 1.683m. These all indicate good correlation between the two data variables. It can be noted here that UAV_{SfM} performs slightly better when compared to ALS_{LiDAR} than when compared to TLS_{LiDAR} when considering R^2. This could be attributed to the fact that both datasets are acquired from airborne vehicles and as such are able to acquire the full top-canopy. The lower RMSE value also signifies that there is lower separation from the line of best fit between the two datasets.

4. Conclusion

The study intended to assess the efficacy of using multi-rotor unmanned aerial vehicles in assessing allometric variables in homogeneous and heterogeneous forest structures necessary for rudimentary biomass estimation using these variables. The unmanned aerial vehicles structure-from-motion (UAV_{SfM}) techniques applied provided fair reconstruction and characterisation of both homogeneous and heterogeneous forest structures, with results being comparable to high-cost LiDAR data obtained from expensive platforms. Overall, UAV_{SfM} provided relatively similar results to LiDAR data when assessing diameter at breast height (DBH), but highly comparative results when

assessing tree height (TH) estimations. Although UAV_{SfM} performed well in TH estimation in this study, CHMs produced can be influenced by the complexity of the top-canopy, and omission of data during the flight capture. As such, additional capture angles, altitudes, flight patterns, high image overlap, multiple-perspective imagery, and capture techniques are necessary to acquire sufficient data to create the stereopairs necessary to reconstruct the captured scene extensively. This means that photogrammetric data cannot deliver the same accuracies as LiDAR data when considering ground cover and below-canopy vegetation conditions without significant effort and relative error but does provide a cheaper alternative. This is evident in previous studies. Further research can be done on the inclusion of tessellated façade imagery in acquiring images for forestry inventory management.

5. References

Agisoft, 2017. Agisoft PhotoScan User Manual. (Professional Edition).

Autodesk, 2021. *ReCap Pro | Reality Capture & 3D Scanning Software | Autodesk*. [online] Available at: <https://www.autodesk.com/products/recap/overview?plc=RECAP&term=1-YEAR&support=ADVANCED&quantity=1> [Accessed 12 Apr. 2021].

Brede, B., Lau, A., Bartholomeus, H.M. and Kooistra, L., 2017. Comparing RIEGL RiCOPTER UAV LiDAR derived canopy height and DBH with terrestrial LiDAR. *Sensors (Switzerland)*, 17(10), pp.1–17.

Carnevali, L., Ippoliti, E., Lanfranchi, F., Menconero, S., Russo, M. and Russo, V., 2018. Close-range MINI-UAVS photogrammetry for architecture survey. *International Archives of the Photogrammetry, Remote Sensing and Spatial Information Sciences - ISPRS Archives*, 42(2), pp.217–224.

Colomina, I. and Molina, P., 2014. Unmanned aerial systems for photogrammetry and remote sensing: A review. *ISPRS Journal of Photogrammetry and Remote Sensing*, 92, pp.79–97.

Dandois, J.P., Olano, M. and Ellis, E.C., 2015. Optimal altitude, overlap, and weather conditions for computer vision uav estimates of forest structure. *Remote Sensing*, 7(10), pp.13895–13920.

DJI, 2017. DJI Phantom 4 Professional User Manual.

DJI, 2021. *DJI GO 4 - Download Center - DJI*. [online] Available at: <https://www.dji.com/downloads/djiapp/dji-go-4> [Accessed 22 Jun. 2021].

Galidaki, G., Zianis, D., Gitas, I., Radoglou, K., Karathanassi, V., Tsakiri–Strati, M., Woodhouse, I. and Mallinis, G., 2017. Vegetation biomass estimation with remote sensing: focus on forest and other wooded land over the Mediterranean ecosystem. *International Journal of Remote Sensing*, 38(7), pp.1940–1966.

González-Jaramillo, V., Fries, A. and Bendix, J., 2019. AGB estimation in a tropical mountain forest (TMF) by means of RGB and multispectral images using an unmanned aerial vehicle (UAV). *Remote Sensing*, 11(12), pp.1–22.

Guerra-Hernández, J., González-Ferreiro, E., Sarmento, A., Silva, J., Nunes, A., Correia, A.C., Fontes, L., Tomé, M. and Díaz-Varela, R., 2016. Using high resolution UAV imagery to estimate tree variables in Pinus pinea plantation in Portugal. *Forest Systems*, 25(2), pp.1–5.

Günlü, A., Ercanli, I., Başkent, E.Z. and Çakır, G., 2014. Estimating aboveground biomass using Landsat TM imagery: A case study of Anatolian Crimean pine forests in Turkey. *Annals of Forest Research*, 57(2), pp.289–298.

Iizuka, K., Yonehara, T., Itoh, M. and Kosugi, Y., 2018. Estimating Tree Height and Diameter at Breast Height (DBH) from Digital surface models and orthophotos obtained with an unmanned aerial system for a Japanese Cypress (Chamaecyparis obtusa) Forest. *Remote Sensing*, 10(1), pp.1–14.

Jayathunga, S., Owari, T. and Tsuyuki, S., 2018. Evaluating the performance of photogrammetric products using fixed-wing UAV imagery over a mixed conifer-broadleaf forest: Comparison with airborne laser scanning. *Remote Sensing*, 10(2), pp.1–24.

Jones, C.L., Weckler, P.R., Maness, N.O., Jayasekara, R., Stone, M.L. and Chrz, D., 2007. Remote Sensing To Estimate Chlorophyll Concentration In Spinach Using Multi-Spectral Plant Reflectance. *American Society of Agricultural and Biological Engineers*, 50(6), pp.2267–2273.

Kachamba, D.J., Eid, T. and Gobakken, T., 2016. Above- and belowground biomass models for trees in the miombo woodlands of Malawi. *Forests*, 7(2).

Kachamba, D.J., Ørka, H.O., Gobakken, T., Eid, T. and Mwase, W., 2016. Biomass estimation using 3D data from unmanned aerial vehicle imagery in a tropical woodland. *Remote Sensing*, 8(11), pp.1–18.

Lenovo, 2020. *Lenovo Y70 Touch | 17.3" Affordable Mobile Laptop | Lenovo US*. [online] Available at: <https://www.lenovo.com/us/en/laptops/lenovo/y-series/y70-touch/> [Accessed 13 Jun. 2020].

Lim, K., Treitz, P., Wulder, M., St-Onge, B. and Flood, M., 2003. LiDAR remote sensing of forest structure. *Progress in Physical Geography*, 27(1), pp.88–106.

Lisein, J., Pierrot-Deseilligny, M., Bonnet, S. and Lejeune, P., 2013. A Photogrammetric Workflow for the Creation of a Forest Canopy Height Model from Small Unmanned Aerial System Imagery. *Forests*, 4(4), pp.922–944.

Maina, E.W., Odera, P.A. and Kinyanjui, M.J., 2017. Estimation of Above Ground Biomass in Forests Using Alos Palsar Data in Kericho and Aberdare Ranges. *Open Journal of Forestry*, 07(02), pp.79–96.

Malone, T., Liang, J. and Packee, E., 2009. *Agriculture Cooperative Alaska Forest Inventory*.

Mlambo, R., Woodhouse, I.H., Gerard, F. and Anderson, K., 2017. Structure from motion (SfM) photogrammetry with drone data: A low cost method for monitoring greenhouse gas emissions from forests in developing countries. *Forests*, 8(3), pp.1–20.

Olofsson, K. and Holmgren, J., 2017a. Tree stem and canopy biomass estimates from terrestrial laser scanning data. In: *International Archives of the Photogrammetry, Remote Sensing and Spatial Information Sciences - ISPRS Archives*. International Society for Photogrammetry and Remote Sensing, pp.157–160.

Pix4Dcapture, 2019. *Pix4Dcapture - Getting Started – Support*. [online] Available at: <https://www.pix4d.com/product/pix4dcapture>.

Puliti, S., 2017. *Use of photogrammetric 3D data for forest inventory Bruk av 3D-data fra fotogrammetri for skogtaksering Philosophiae Doctor (PhD) Thesis Norwegian University of Life Sciences*.

Puliti, S., Ørka, H.O., Gobakken, T. and Næsset, E., 2015. Inventory of small forest areas using an unmanned aerial system. *Remote Sensing*, 7(8), pp.9632–9654.

SACAA, 2021. *General Information*. [online] Available at: <http://caa.co.za/Pages/RPAS/Remotely Piloted Aircraft Systems.aspx> [Accessed 11 Apr. 2021].

St-Onge, B., Vega, C., Fournier, R.A., Hu, Y., Vega{, C. and Hu{, Y., 2008. Mapping canopy height using a combination of digital stereo-photogrammetry and lidar. *nternational Journal of Remote Sensing*, 29(11), pp.3343–3364.

Trimble Geospatial, 2021. *Trimble Business Center | Trimble Geospatial*. [online] Trimble Geospatial. Available at: <https://geospatial.trimble.com/products-and-solutions/trimble-business-center> [Accessed 11 Apr. 2021].

Tuswa, N., Bugan, R.D.H., Mapeto, T., Jovanovic, N., Gush, M., Kapangaziwiri, E., Dzikiti, S., Kanyerere, T. and Xu, Y., 2019. The impacts of commercial plantation forests on groundwater recharge: A case study from George (Western Cape, South Africa). *Physics and Chemistry of the Earth*, 112(December), pp.187–199.

Wilkes, P., Lau, A., Disney, M., Calders, K., Burt, A., Gonzalez de Tanago, J., Bartholomeus, H., Brede, B. and Herold, M., 2017. Data acquisition considerations for Terrestrial Laser Scanning of forest plots. *Remote Sensing of Environment*, 196, pp.140–153.

Zoller + Fröhlich, 2020. *ZF-Laser - Z+F IMAGER® 5010X, 3D Laser Scanner*. [online] Available at: <https://www.zf-laser.com/Z-F-IMAGER-R-5010X.3d_laser_scanner.0.html?&L=1> [Accessed 9 Apr. 2020].

Zoller + Fröhlich, 2020. *ZF-Laser - Z+F LaserControl*®. [online] Available at: <https://www.zf-laser.com/Z-F-LaserControl-R.laserscanner_software_1.0.html?&L=1> [Accessed 20 Nov. 2020].